Small

NANO · MICRO small
www.small-journal.com

RESEARCH ARTICLE OPEN ACCESS

Supercapacitive Carbon-Coated δ-MnO_2 Nanosheets as a Solid-Contact Material for Self-Testing Potassium-Ion Biosensors

Jaeyeon Lee[1] | Chaeeun Kim[2] | Chaehyung Kim[2] | Yujoon Kim[2] | Seojin Lee[1] | Kangwon Lee[2] | In Young Kim[1]

[1]Department of Chemistry and Nano Sciences, Ewha Womans University, Seoul, Republic of Korea | [2]Department of Applied Bioengineering, Seoul National University, Seoul, Republic of Korea

Correspondence: Kangwon Lee (kangwonlee@snu.ac.kr) | In Young Kim (iykim@ewha.ac.kr)

Received: 29 October 2025 | **Revised:** 30 January 2026 | **Accepted:** 5 March 2026

Keywords: carbon coating | ion-sensing kinetics | manganese oxides | oxamide | solid-contact ion selective electrodes | supercapacitors

ABSTRACT

Carbon-coated δ-MnO_2 nanosheets (δ-MnO_2@C) are developed as a solid-contact material for all-solid-state potassium-ion biosensors. The synthesis is designed to be facile and scalable: manganese(II) acetate and oxamide are coprecipitated and subsequently oxidized by persulfate treatment, achieving simultaneous crystallization of δ-MnO_2 and carbon coating in a one-pot process at room temperature. Benefiting from their large specific surface area, efficient redox activity, and good electrical conductivity, δ-MnO_2@C exhibits a high specific capacitance of 165.9 F g^{-1} at 1.0 A g^{-1} when used as an electrode material for supercapacitors. Practical biosensing applicability is demonstrated by employing δ-MnO_2@C as a solid-contact material into a potassium-ion sensing strip, enabling accurate detection of K^+ concentrations across a wide range (1.0×10^{-4} - 1.0×10^{-1} M). Notably, δ-MnO_2@C-employed potentiometric potassium-ion sensor achieved 1.4-fold faster response time compared with conventional activated carbon contacts. Comparative studies reveal that sensor response time is governed primarily by the areal capacitance of the solid-contact material rather than its surface area or porosity. Owing to the simplicity of the synthesis and the superior performance, δ-MnO_2@C provides a promising pathway toward portable self-testing potassium-ion biosensors for daily monitoring of blood potassium levels in patients with renal failure.

1 | Introduction

Acute renal failure is characterized by the sudden loss of kidney function, leading to the accumulation of metabolic waste products and excess fluid in the body [1]. In contrast, chronic renal failure refers to a persistent and progressive decline in kidney function that ultimately necessitates renal replacement therapy [2]. Globally, more than 800 million people are affected by chronic renal failure, highlighting an urgent need for simple and effective strategies for disease prevention and long-term management [3]. Potassium ions (K^+) play a critical role in muscle contraction and nerve signal transmission [4]. However, deviations of serum potassium concentrations from the normal physiological range (3.50–5.59 mEq L^{-1}) can induce severe complications, including muscle paralysis, respiratory failure, and cardiac arrest, which may result in sudden death [4–6]. Therefore, portable self-testing biosensors capable of accurately monitoring blood potassium levels using only a small drop of blood, anytime and anywhere, are of great importance for patients with chronic renal failure [7].

Potassium-ion-selective electrodes (K^+-ISEs) are typically based on potentiometric principles, in which the potassium-ion concentration is determined from the potential difference between an ion-selective electrode and a reference electrode, as described

by the Nernst equation [8]. Conventional K^+-ISEs rely on liquid-phase electrolytes [7, 8], rendering them unsuitable for portable applications because of bulky device configurations and leakage concerns. To overcome these limitations, solid-contact materials have been introduced to replace the internal liquid electrolyte with a solid-state interface [9]. By establishing intimate contact between the ion-selective membrane and the electronic conductor, solid-contact layers enable sensor miniaturization and significantly improve potential stability [10]. For optimal performance, the solid-contact layer must efficiently transduce ionic signals into electronic signals without inducing potential drift [11].

Conducting polymers, including polypyrroles, polythiophenes, and polyanilines, were among the earliest materials employed as solid-state ion-to-electron transducers. Partially p- or n-doped conducting polymers generate electronic signals through redox reactions triggered by ionic fluxes [11]. However, their redox potentials are highly sensitive to parasitic redox processes, such as water penetration and oxygen interference, leading to poor long-term potential stability [11]. Carbon-based materials exhibit lower sensitivity to water penetration due to their intrinsic hydrophobicity. Accordingly, nanostructured carbons, such as graphene, carbon nanotube (CNT), and activated carbon, have been extensively investigated as alternative solid-contact materials that transduce ions to electrons via electric double-layer capacitance (EDLC) [12, 13]. Despite these advantages, all-solid-state K^+-ISEs employing nanostructured carbons as solid contacts often suffer from slow response kinetics [14]. Moreover, graphene and CNT require costly and energy-intensive synthesis processes. These limitations motivate the exploration of alternative solid-contact materials that combine rapid sensing response with low production cost.

Inorganic compounds such as RuO_2, IrO_2, $NiCo_2S_4$, MoO_2, WO_3, and MnO_2 exhibit high pseudocapacitance, making them attractive candidates for solid-contact layers in all-solid-state K^+-ISEs [15–21]. Among these materials, MnO_2 is particularly appealing due to its low cost, non-toxicity, and natural abundance. Nevertheless, the application of MnO_2-based materials in all-solid-state potassium-ion biosensors remains largely unexplored [22, 23]. Komaba et al. focused on the intercalation chemistry of birnessite-type manganese dioxide (δ-MnO_2) [22]. They reported that near-Nernstian behavior was observed when δ-MnO_2 served as a solid-contact layer beneath a potassium-ion-selective ionophore membrane, whereas potentiometric responses deviated from Nernstian behavior when δ-MnO_2 was used directly as a potassium-ion sensing material. The same group subsequently developed a poly(allylamine)–δ-MnO_2 composite and demonstrated its effectiveness as a solid-contact material for anion sensing, including Cl^- and NO_3^- [23].

To the best of our knowledge, no prior study has reported the use of carbon-coated δ-MnO_2 nanosheets as solid-contact materials for all-solid-state K^+-ISEs. Carbon coating can enhance the pseudocapacitance of δ-MnO_2 nanosheets by facilitating electron transport across the grain boundary of δ-MnO_2 [24]. In addition, the carbon layer transforms the intrinsically hydrophilic surface of δ-MnO_2 into a more hydrophobic one [24], which is critical for suppressing water-layer formation at the ion-selective membrane/solid-contact interface in solid-contact ion-selective electrodes [23]. For practical single-use all-solid-state K^+-ISE strips, the synthesis of carbon-coated δ-MnO_2 nanosheets must be simple, cost-effective, and energy-efficient. Previously reported methods for producing carbon-coated MnO_2 typically involve energy-intensive, multistep procedures and often yield non-uniform carbon layers [25]. To address these challenges, we developed a facile one-pot strategy for synthesizing carbon-coated δ-MnO_2 nanosheets (denoted as δ-MnO_2@C). In this approach, oxamide functions as an efficient carbon-coating precursor during the crystal growth of δ-MnO_2 at room temperature, enabling an exceptionally simple and energy-efficient synthesis. Owing to multifunctionality of δ-MnO_2@C, its performance was systematically evaluated both as a supercapacitor electrode and as a solid-contact layer in all-solid-state potassium-ion biosensors. Through this dual investigation, we elucidated the correlation between interfacial capacitance and sensing kinetics, thereby establishing δ-MnO_2@C as a promising solid-contact material for portable potassium-ion biosensing applications.

2 | Results and Discussion

2.1 | Crystal Structure and Morphology

The crystal structure of δ-MnO_2@C was examined by X-ray diffractometry (XRD), as shown in Figure 1a. The sample exhibits (001), (002), (100), and (110) reflections corresponding to the crystal planes of birnessite-type δ-MnO_2 (COD Card No. 9013650, space group C-1) [26], indicating that Mn^{2+} ions were oxidized during persulfate treatment to form δ-MnO_2 [27]. No reflection peaks related to oxamide are observed. The morphology of the sample was investigated by field-emission scanning electron microscopy (FE-SEM), as presented in Figure 1b. δ-MnO_2@C displays a nanoflower-like morphology, attributable to assemblies of δ-MnO_2 nanosheets with a lateral size of approximately 500 nm. Numerous mesopores are present within the nanosheet assemblies.

The surface area and pore structure of δ-MnO_2@C were further characterized by N_2 sorption at 77 K. As shown in Figure 1c, δ-MnO_2@C exhibits a type-IV isotherm with an H3-hysteresis loop [28]. The type-IV isotherm indicates the presence of mesopores, while the H3-hysteresis loop suggests groove-like mesopores formed by flaky frameworks [27, 29]. This mesoporous structure results in an expanded Brunauer–Emmett–Teller (BET) surface area of 122.2 $m^2\ g^{-1}$. The average mesopore size was determined to be 35.5 nm (Figure S1). These mesoporous characteristics observed by N_2 sorption are consistent with the FE-SEM results. The large surface area and well-developed mesoporous structure of δ-MnO_2@C contribute to its high specific capacitance.

High-resolution transmission electron microscopy (HR-TEM) confirms the successful carbon coating on δ-MnO_2 nanosheets, as shown in Figure 1d. Two distinct lattice fringes with *d*-spacings of 0.381 and 0.243 nm are observed in the HR-TEM image of δ-MnO_2@C, corresponding to the (002) planes of graphite and the (100) planes of δ-MnO_2, respectively [26, 30]. The long-range alignment of δ-MnO_2 (100) lattices surrounded by carbon (002) planes demonstrates the successful oxamide-derived carbon coating on δ-MnO_2 nanosheets. A low-magnification TEM image (Figure S2) further proves the uniform and thin carbon

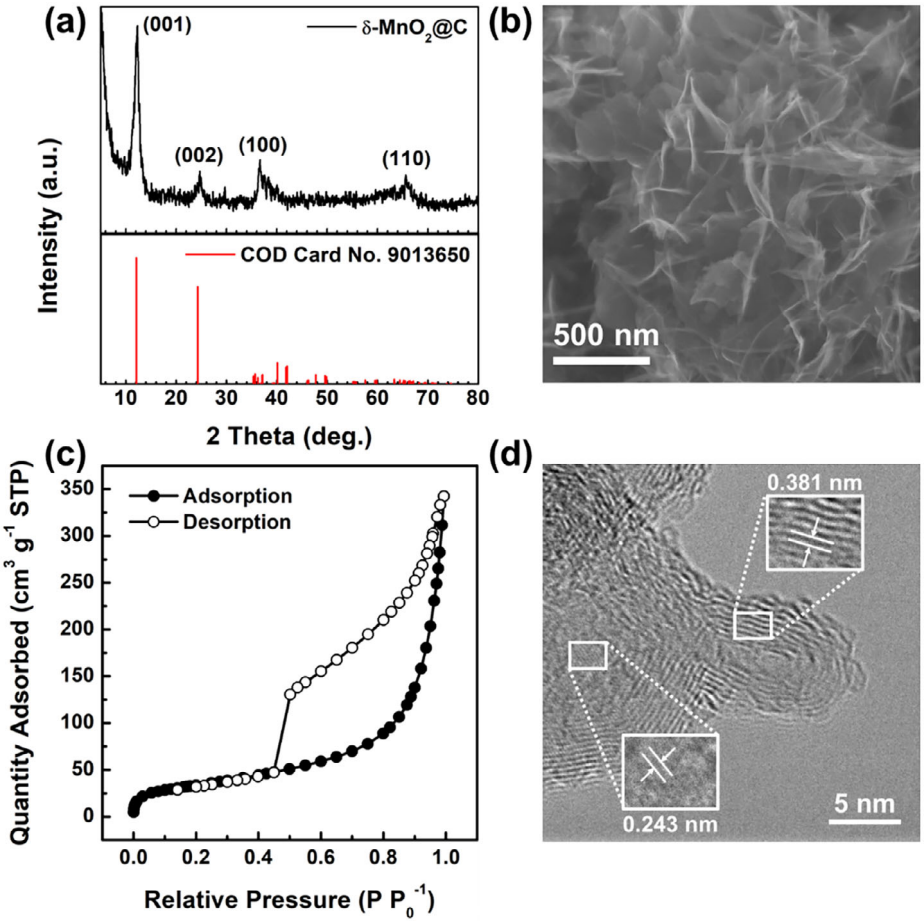

FIGURE 1 | (a) Powder XRD pattern, (b) FE-SEM image, (c) N_2 adsorption-desorption isotherm at 77 K, and (d) HR-TEM image of δ-MnO_2@C.

coating on δ-MnO_2. A cross-sectional TEM image (Figure S3) shows that the thicknesses of the carbon layer and δ-MnO_2 are approximately 5.5–6.7 and 11 nm, respectively. This uniform and thin carbon coating layer can effectively facilitate electron transfer across δ-MnO_2@C, enhancing its performance as both an electrode material for supercapacitors and a solid-contact material for potassium-ion biosensors [23, 24]. The carbon content determined by CHNS elemental analysis is 2.46wt%. Micro-Raman spectroscopy was performed for δ-MnO_2@C to quantify the degree of graphitization of the carbon layer. However, no discernible Raman signal attributable to carbon was observed (Figure S4), which is likely due to the extremely thin carbon layer (<10 nm) [31]. At such thickness, Raman detection of carbon is inherently challenging. To the best of our knowledge, this is the first report demonstrating the efficacy of oxamide as a carbon source for coating metal oxides. The mechanism of Mn^{2+} oxidation by persulfate ($S_2O_8^{2-}$) at room temperature is described as follows [27, 32].

$$Mn^{2+}(aq) + S_2O_8^{2-}(aq) + 2H_2O(l) \rightarrow \delta - MnO_2(s) + 2SO_4^{2-}(aq) + 4H^+(aq)$$

Simultaneously, the persulfate ($S_2O_8^{2-}$) is activated into sulfate radicals ($SO_4^{\bullet-}$) by Mn^{2+} as shown below [33].

$$Mn^{2+}(aq) + S_2O_8^{2-}(aq) \rightarrow Mn^{3+}(aq) + SO_4^{\cdot-}(aq) + SO_4^{2-}(aq)$$

It is inferred that oxamide ($(CONH_2)_2$) is predominantly oxidized by the sulfate radicals ($SO_4^{\bullet-}$) while oxamide coordinated on the surface of δ-MnO_2 nanosheets is converted into carbon species that remain on the δ-MnO_2 surface [34–36]. As shown in Figure S5, oxamide does not react with persulfate in the absence of δ-MnO_2, which supports that δ-MnO_2 accelerates the formation of sulfate radicals ($SO_4^{\bullet-}$) and fixes carbon species derived from oxamide, leading to the formation of a carbon layer on the surface of δ-MnO_2 nanosheets.

2.2 | Surface Features

The bonding features of the carbon coating layer were analyzed by Fourier-transform infrared (FT-IR) spectroscopy (Figure 2a). FT-IR spectra of oxamide and δ-MnO_2@C were compared to determine whether unreacted oxamide remained in the product. Oxamide shows C–N stretching vibrations at 1343, 1295, and 1092 cm^{-1}, as well as C = O stretching bands at 1647 and 1607 cm^{-1} [37]. A C–H bending mode is also observed at 792 cm^{-1} [38]. These characteristic C–N and C = O signals at 1343, 1092, and 1647 cm^{-1} are absent in δ-MnO_2@C, confirming the complete decomposition of oxamide. Instead, δ-MnO_2@C exhibits C = C stretching vibrations at 1666 and 1620 cm^{-1} [39], indicating the formation of graphitic carbon. This observation is consistent with the HR-TEM results, which revealed (002) lattice planes of graphite. An additional O–H/C–H bending feature at 1414 cm^{-1}

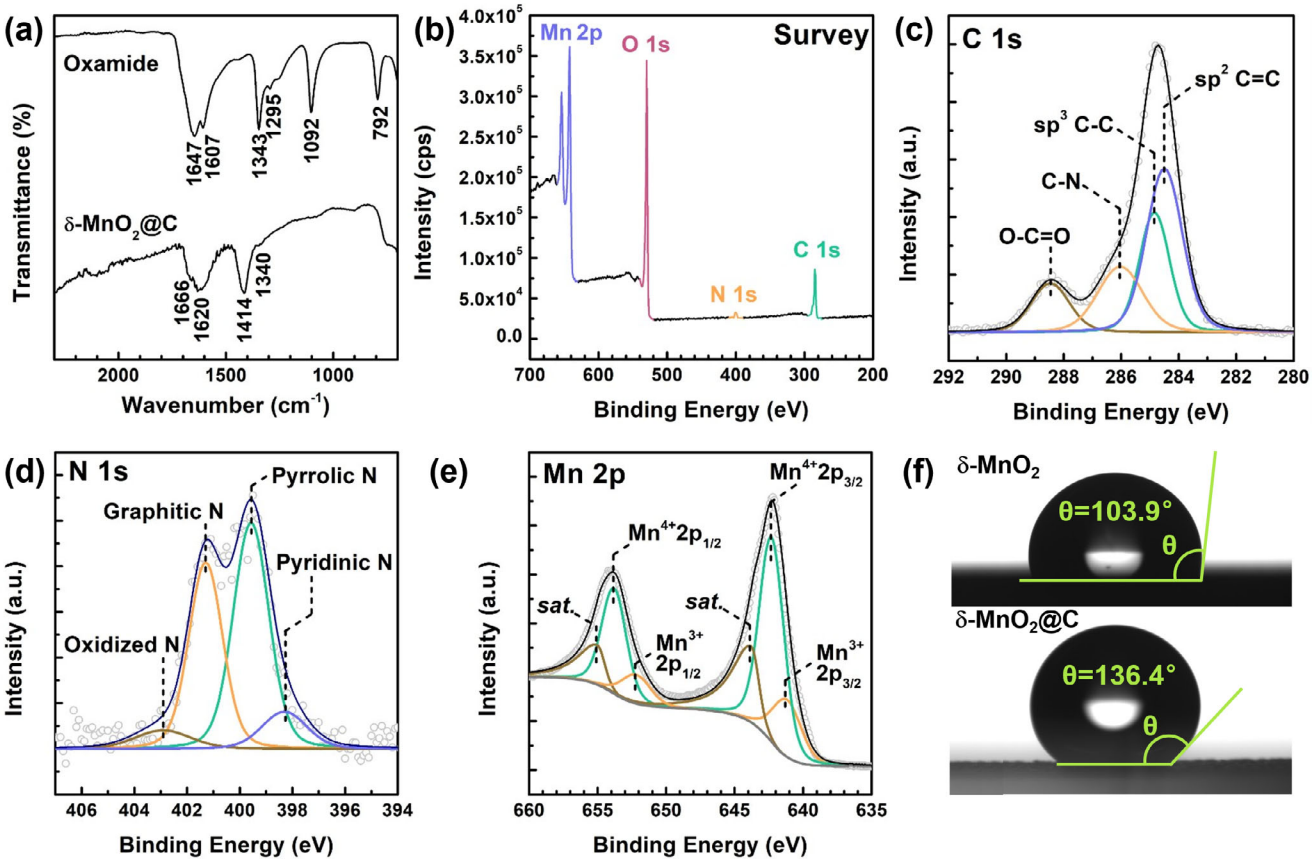

FIGURE 2 | (a) FT-IR spectra of oxamide and δ-MnO_2@C, (b) survey and high resolution (c) C 1s, (d) N 1s, and (e) Mn 2p XPS spectra of δ-MnO_2@C, and (f) contact angles of a water droplet on the surfaces of δ-MnO_2 (top) and δ-MnO_2@C (bottom).

can be attributed to functional groups within the carbon coating [40]. A weak band at 1340 cm^{-1} suggests the presence of graphitic N in δ-MnO_2@C [41].

X-ray photoelectron spectroscopy (XPS) further confirmed nitrogen incorporation in δ-MnO_2@C with an atomic N/C ratio of 0.063 (Figure 2b and Table S1). The XPS and FT-IR results demonstrate the formation of an N-doped carbon coating layer on δ-MnO_2. High-resolution XPS spectra of C 1s, N 1s, and Mn 2p for δ-MnO_2@C are shown in Figure 2c–e. The C 1s spectrum was deconvoluted into four components assigned to sp^2 C = C (284.5 eV), sp^3 C–C (284.8 eV), C–N (286.0 eV), and O–C = O (288.5 eV) bonds [42, 43]. The strong sp^2 C = C peak provides further evidence of graphitization. The C–N peak confirms N-doping, while O–C = O is attributed to surface oxidation. The sp^3 C–C contribution likely arises from amorphous carbon and unavoidable surface contamination. The graphitic-to-amorphous carbon ratio has been quantified by deconvolution of the C1s XPS spectra into sp^2 C = C and sp^3 C–C components. The pronounced sp^2 C = C peak indicates a significant degree of graphitization, whereas the sp^3 C–C contribution originates from amorphous carbon as well as unavoidable surface contamination inherent to XPS measurements. Based on the areal ratio of $A_{sp2}/(A_{sp2}+A_{sp3})$ of 0.619, the graphitic carbon fraction in the carbon layer is conservatively estimated to be at least 61.9%. The N 1s spectrum was fitted with four peaks at 398.3, 399.6, 401.3, and 402.9 eV, corresponding to pyridinic, pyrrolic, graphitic, and N–O species, respectively [44, 45]. The dominant pyrrolic N fraction is attributed to the relatively low synthesis temperature of δ-MnO_2@C. Pyrrolic N is known to enhance pseudocapacitance by providing electrochemically active sites for cation storage via local polarization [46]. The Mn 2p spectrum reveals manganese predominantly in the +4 oxidation state, consistent with MnO_2 [47]. A minor Mn^{3+} component is also detected, likely originating from partial reduction of Mn^{4+} in contact with the electron-rich carbon layer [48], further evidencing intimate carbon coating on δ-MnO_2.

Because surface-property modification was anticipated after carbon coating, contact-angle measurements were performed on δ-MnO_2 and δ-MnO_2@C. As shown in Figure 2f, δ-MnO_2@C exhibits a water contact angle of 136.4°, significantly larger than that of non-coated δ-MnO_2 (103.9°). This indicates that the carbon coating confers hydrophobicity to the surface. Such hydrophobic modification helps prevent water penetration between the solid-contact material and the potassium-ion selective membrane, thereby improving the chemical stability of the all-solid-state potassium-ion biosensors [23, 49].

2.3 | Supercapacitance

To evaluate the supercapacitive performance of δ-MnO_2@C and its potential as an electrode material, cyclic voltammetry (CV) and galvanostatic charge–discharge measurements were carried out between -0.100 and 0.900 V vs. Ag/AgCl in 1.0 M Na_2SO_4

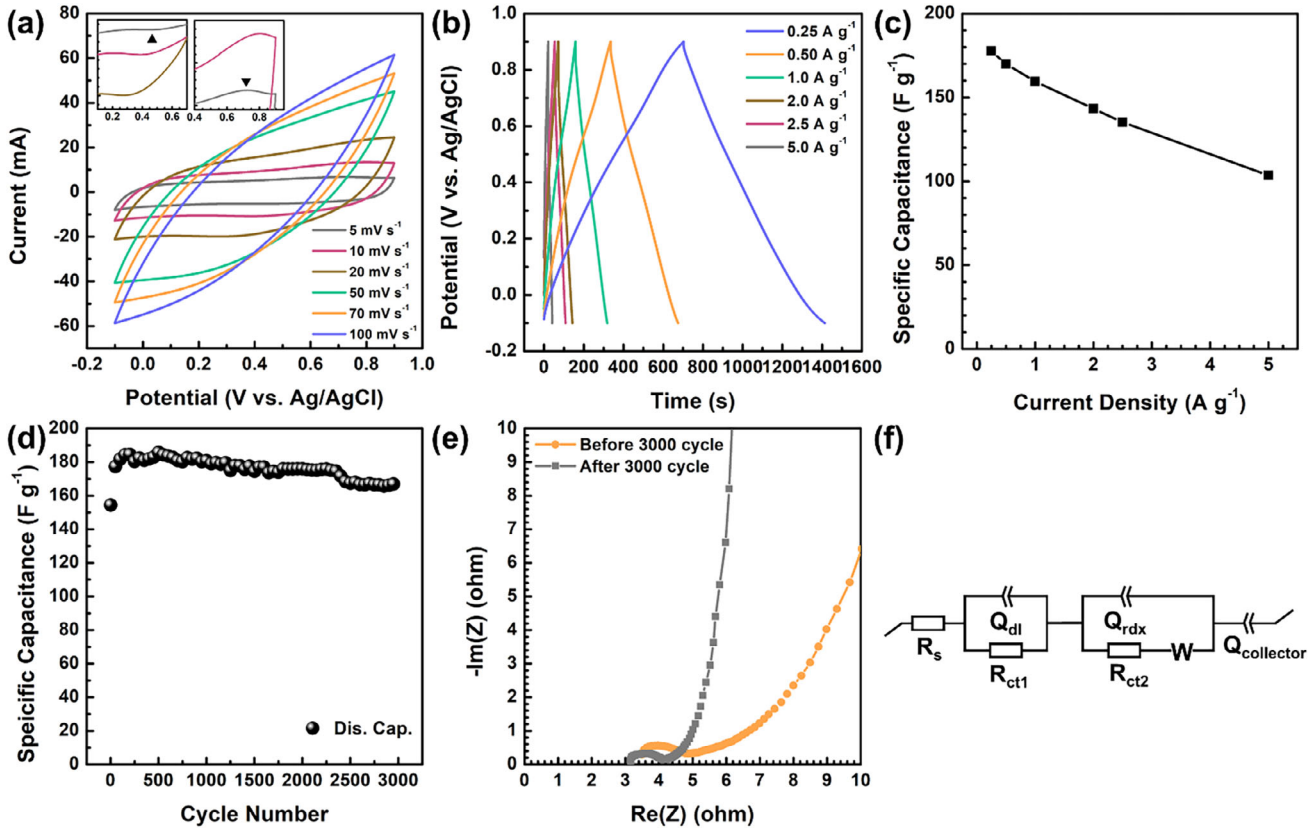

FIGURE 3 | (a) CV curves at scan rates of 5, 10, 20, 50, 70, and 100 mV s^{-1}, (b) galvanostatic charge-discharge curves and (c) specific discharge capacitances at current densities of 0.25, 0.50, 1.0, 2.0, 2.5, and 5.0 A g^{-1}, (d) cyclability at 1.0 A g^{-1}, (e) Nyquist plots at open circuit potential before and after 3000 cycles, and (f) equivalent circuit for δ-MnO_2@C in 1.0 M Na_2SO_4 electrolyte. Insets in (a) show magnified CV curves highlighting the reduction and oxidation peaks at 0.478 and 0.726 V vs. Ag/AgCl, respectively.

electrolyte. As shown in Figure 3a, the CV curves of δ-MnO_2@C exhibit a nearly rectangular shape with distinct reduction and oxidation peaks across a wide scan-rate range of 5–20 mV s^{-1}. These features indicate that the capacitance of δ-MnO_2@C originates from both EDLC and Faradaic redox reactions [50]. The redox peaks at 0.478 and 0.726 V vs. Ag/AgCl correspond to the following reversible processes [50, 51]:

$$MnO_2\,(s) + Na^+\,(aq) + e^- \rightarrow MnOONa\,(s) \quad (0.478\ \text{V vs. Ag/AgCl})$$

$$MnOONa\,(s) \rightarrow MnO_2\,(s) + Na^+\,(aq) + e^- \quad (0.726\ \text{V vs. Ag/AgCl})$$

The redox peaks disappear at higher scan rates above 50 mV s^{-1}, which results from the increased polarization of the electrode at high scan rates [52].

The galvanostatic charge–discharge profiles (Figure 3b) display linear and symmetric triangular shapes, confirming the excellent reversibility and capacitive nature of δ-MnO_2@C over the entire range of tested current densities. The specific capacitances of samples were calculated in both gravimetric and areal terms and are summarized in Table S2. The gravimetric specific capacitance of δ-MnO_2@C is 177.7, 169.9, 159.5, 143.4, 135.3, and 103.5 F g^{-1} at current densities of 0.25, 0.50, 1.0, 2.0, 2.5, and 5.0 A g^{-1}, respectively. Notably, δ-MnO_2@C delivers significantly higher capacitance compared with activated carbon (Figure S6), which is primarily attributable to the Faradaic contribution from MnO_2. As plotted in Figure 3c, the decreases in specific capacitances with increasing current density are not significant, demonstrating excellent rate capability and electrochemical stability. Long-term cycling stability of δ-MnO_2@C was further evaluated (Figure 3d). An increase in specific capacitance during the initial 50 cycles is ascribed to the formation of stable ion-migration pathways. Afterward, δ-MnO_2@C maintains a capacitance above 165.9 F g^{-1} at 1.0 A g^{-1} even after 3000 cycles, highlighting its outstanding durability. The gravimetric specific capacitance values of the facilely synthesized δ-MnO_2@C are comparable to those of MnO_2-based electrode materials reported to date, as summarized in Table S3.

Electrochemical impedance spectroscopy (EIS) was conducted to investigate the charge-transfer dynamics and resistances of δ-MnO_2@C (Figure 3e). The Nyquist plot of δ-MnO_2@C before cycling exhibits a semicircle in the high- and mid-frequency regions, followed by a straight line in the low-frequency region. The plot was well fitted using the equivalent circuit shown in Figure 3f (Table S4). The Nyquist plot is more accurately described using the constant phase elements (Q), which account for the non-ideal capacitive behavior commonly observed in real electrochemical systems including coated materials, rather than ideal capacitors (C). In this circuit, R_s represents the electrolyte resistance. Following R_s, the EDLC-related components include the charge-transfer resistance (R_{ct1}) and the constant phase

element associated with the EDLC (Q_{dl}). The Faradaic processes are subsequently followed by R_{ct2}, the redox capacitance (Q_{rdx}) and the Warburg impedance (W). W reflects ion diffusion during the Faradaic processes. The final constant phase element ($Q_{collector}$) in the equivalent circuit corresponds to the non-ideal capacitive behavior of the Ni foam used as a porous current collector [53].

The small R_{ct} values corresponding to the small semicircle indicate efficient charge transfer during both EDLC and Faradaic processes in δ-MnO_2@C, reflecting its good electrical conductivity. Meanwhile, the straight line with an approximately 45° slope confirms the ion-diffusion-controlled Warburg impedance characteristic of δ-MnO_2@C [54]. These features are consistent with the pseudocapacitive behavior of δ-MnO_2@C. Notably, after 3000 cycles, the charge-transfer resistance is markedly reduced and the Warburg impedance becomes steeper, indicating the formation of percolated ion-transport pathways both at the material interfaces and within the crystal lattices of δ-MnO_2@C during cycling [54]. The consistent overall shape of the Nyquist plots before and after cycling further highlights the robustness of δ-MnO_2@C as an electrode material for supercapacitors.

Since δ-MnO_2@C undergoes both EDLC and Faradaic processes during cycling, their respective contributions to total capacity were analyzed using Dunn's method to provide deeper mechanistic insight and to establish the relevance of the charge-storage mechanism to sensor response. Dunn's method enables quantitative separation of capacitive and diffusion-controlled contributions at specific potentials. As shown in Figure S7, charge storage in δ-MnO_2@C at a scan rate of 5 mV s^{-1} arises from both EDLC (60.06%) and Faradaic (39.94%) processes. The EDLC contribution increases with increasing scan rate, consistent with trends widely reported for nanostructured electrodes [55]. Notably, the diffusion-controlled contribution in δ-MnO_2@C (24.95–39.94%) is approximately twice that observed for activated carbon (11.28–20.27%) across scan rates of 20, 10, and 5 mV s^{-1}.

2.4 | Potassium Ion-Dependent Amperometry

The electrochemical response of δ-MnO_2@C to potassium ions was investigated via CV at varying potassium-ion concentrations. For the CV measurements, a δ-MnO_2@C-loaded glassy carbon electrode served as the working electrode, while buffer solutions (pH 7.4) containing KCl (2.0–7.0 mM) were used as the electrolyte to mimic the physiological environment, as illustrated in Figure 4a [56]. Considering that the normal potassium-ion range in human blood is 3.50–5.59 mM, the tested concentration range of 2.0–7.0 mM sufficiently covers the biologically relevant range for potassium-ion monitoring [11].

The redox features observed in the CV curves of δ-MnO_2@C in buffer (Figure 4b) resemble those obtained in Na_2SO_4 solution (Figure 3a), displaying quasi-rectangular shapes with small reduction and oxidation peaks at approximately -0.115 and 0.481 V vs. Ag/AgCl, respectively [57]. The redox current of δ-MnO_2@C increases proportionally with potassium-ion concentration, indicating its high sensitivity to potassium ions. The consistent potassium-ion storage behavior of δ-MnO_2@C in buffer enabled amperometric analysis as a function of potassium-ion concentration. Anodic current values at 0.481 V vs. Ag/AgCl were used for potassium ion-dependent amperometric calibration. The resulting calibration curve (Figure 4c) shows a linear relationship between potassium-ion concentration and anodic current, with a high correlation coefficient of $R^2 = 0.9938$. Given that a solid-contact material is required to convert potassium-ion signals into electronic signals [22], the linear amperometric response of δ-MnO_2@C confirms that it can effectively transduce potassium-ion signals to electric current as a solid-contact material in all-solid-state potentiometric potassium-ion biosensors.

2.5 | Potentiometric Potassium-Ion Sensors

A portable all-solid-state potentiometric potassium-ion biosensor was fabricated including a sensing strip, as displayed in Figure 5a. The strip employs a compact two-electrode configuration, consisting of a working and a reference electrode. In the working electrode, δ-MnO_2@C is positioned between the potassium-ion selective membrane (K^+-ISM) and the electrical conducting point as illustrated in Figure 5b [11]. The roles of δ-MnO_2@C as a solid-contact material can be classified into two main functions: (1) transduction of the potassium-ion signal into an electronic signal and (2) suppression of potential drift arising from changes in the chemical environment. The first role is schematically described in Figure 5b. When potassium ions are selectively captured by the K^+-ISM, charge transfer at the membrane/solid-contact interface is required to generate an electronic response. This process has often been interpreted as involving ion (K^+) or counter-ion (R^-) transfer into the solid-contact layer accompanied by redox reactions of the inorganic material, thereby generating electron flow [11].

The sensing validity and response kinetics of the sensing strip employing δ-MnO_2@C as the solid-contact material were evaluated by chronopotentiometry using the portable potentiometer shown in Figure 5a. Equilibrium was defined as the point at which ΔE remained within ±0.1 mV for 10 s. To assess the sensing performance, phosphate-buffered saline (PBS) solution containing K^+ ranging from 1.0×10^{-9} to 3.0×10^{0} M was dropped onto the sensing strip. The open-circuit potential between the working and reference electrodes was measured, thereby establishing the valid calibration range of the sensing strip. An advantage of this all-solid-state potentiometric potassium-ion biosensor lies in its minimal sample requirement: only 10.0 µL of sample is sufficient for analysis, making it particularly suitable for point-of-care testing.

As shown in Figure 5c, the open circuit potential versus $\log a_{K^+}$ graph exhibits a linear plot with the slope value of 0.0624 within the a_{K^+} range of 1.0×10^{-4} – 1.0×10^{-1} M. The measured slope value is quite close to the ideal slope value of 0.0592 obeying the Nernst equation (Equation (1)):

$$E\,(\mathrm{V}) = E^{\circ} - 0.0592 \log\, a_x \left(25^{\circ}\mathrm{C}\right) \quad (1)$$

where E and E° are the observed and standard redox potentials (V), respectively, and a_x corresponds to the molarity of potassium ion [8, 58]. The open-circuit potentials below 1.0×10^{-4} M and above 1.0×10^{-1} M do not obey the Nernst equation. From this result, the sensing strip exhibits a broad valid calibration range

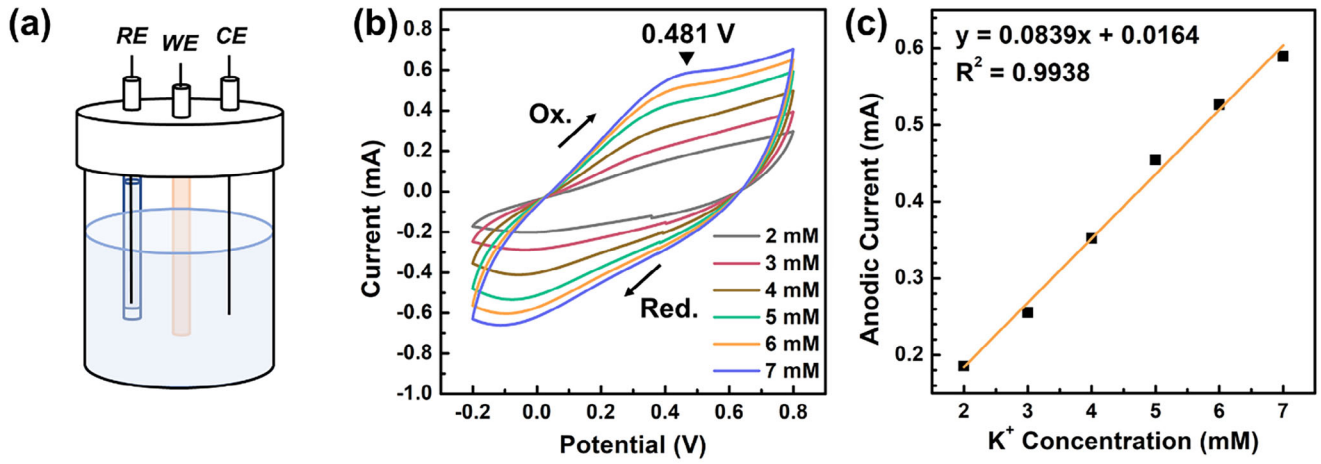

FIGURE 4 | (a) Schematic depicting a three-electrode system for amperometry, (b) CV graphs of δ-MnO_2@C in tris-HCl buffer solutions containing KCl (2.0–7.0 mM) at a scan rate of 50 mV s^{-1}, (c) potassium ion-dependent amperometric calibration curve at 0.481 V vs. Ag/AgCl for δ-MnO_2@C.

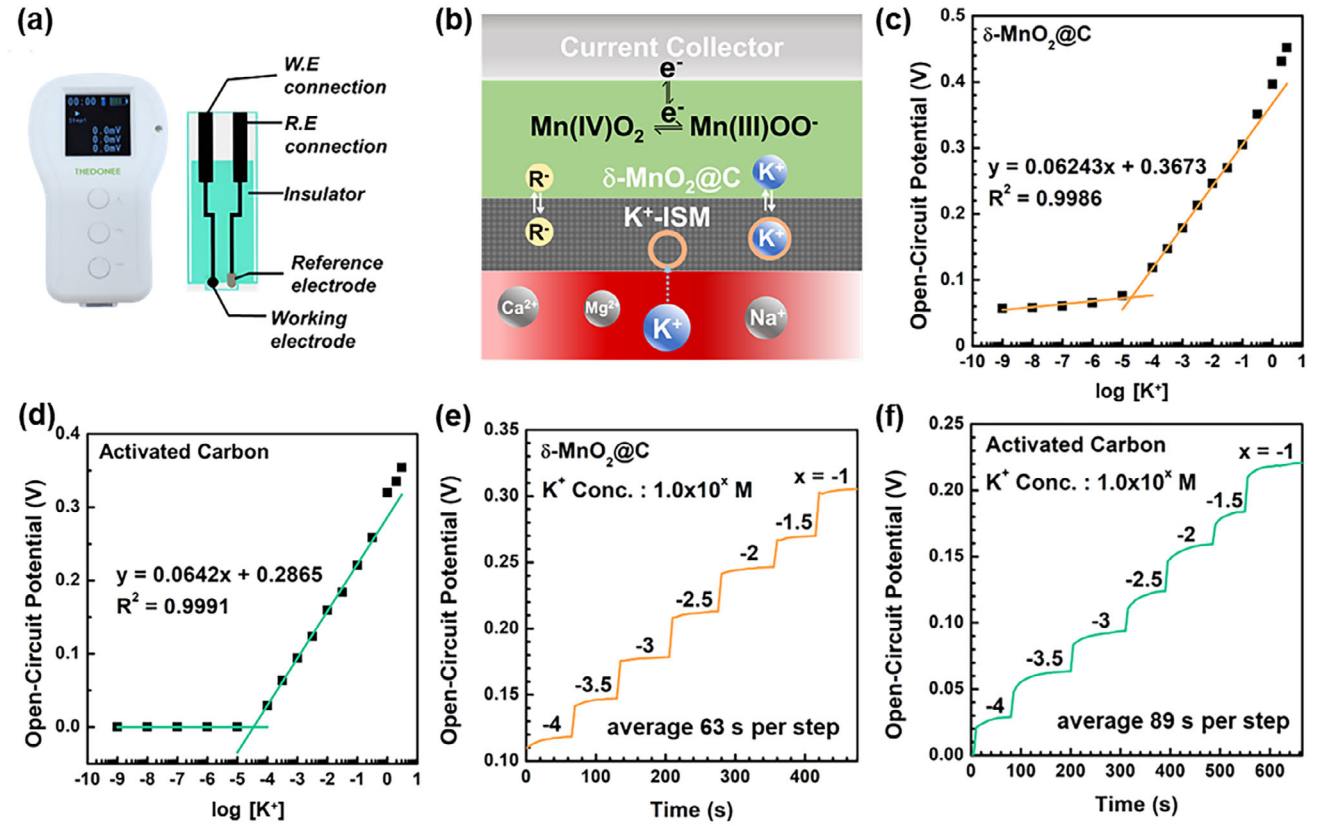

FIGURE 5 | (a) A photo image of the portable potentiometric potassium-ion biosensor with a sensing strip, (b) schematic representation of the working electrode, open-circuit potential versus loga_{K+} graphs recorded on the sensing strips employing (c) δ-MnO_2@C and (d) activated carbon, and chronopotentiometric response curves recorded on the sensing strips employing (e) δ-MnO_2@C and (f) activated carbon.

within $1.0 \times 10^{-4} - 1.0 \times 10^{-1}$ M including biologically relevant concentration of approximately $3.50 \times 10^{-3} - 5.59 \times 10^{-3}$ M.

The response kinetics of the sensing strip employing δ-MnO_2@C were compared with the sensing strip employing activated carbon as the solid-contact material. The activated carbon-based sensing strip presents only a valid calibration range within $1.0 \times 10^{-4} - 1.0 \times 10^{-2}$ M K^+ (Figure 5d). Notably, the δ-MnO_2@C-based sensing strip demonstrates a significantly faster response across the valid potassium-ion concentration range ($1.0 \times 10^{-4} - 1.0 \times 10^{-1}$ M K^+) as shown in Table S5. The equilibrium was achieved within average 63 s with δ-MnO_2@C (Figure 5e), markedly 1.4-fold faster than the average 89 s required with conventional activated carbon (Figure 5f). δ-MnO_2@C effectively overcomes the slow kinetics

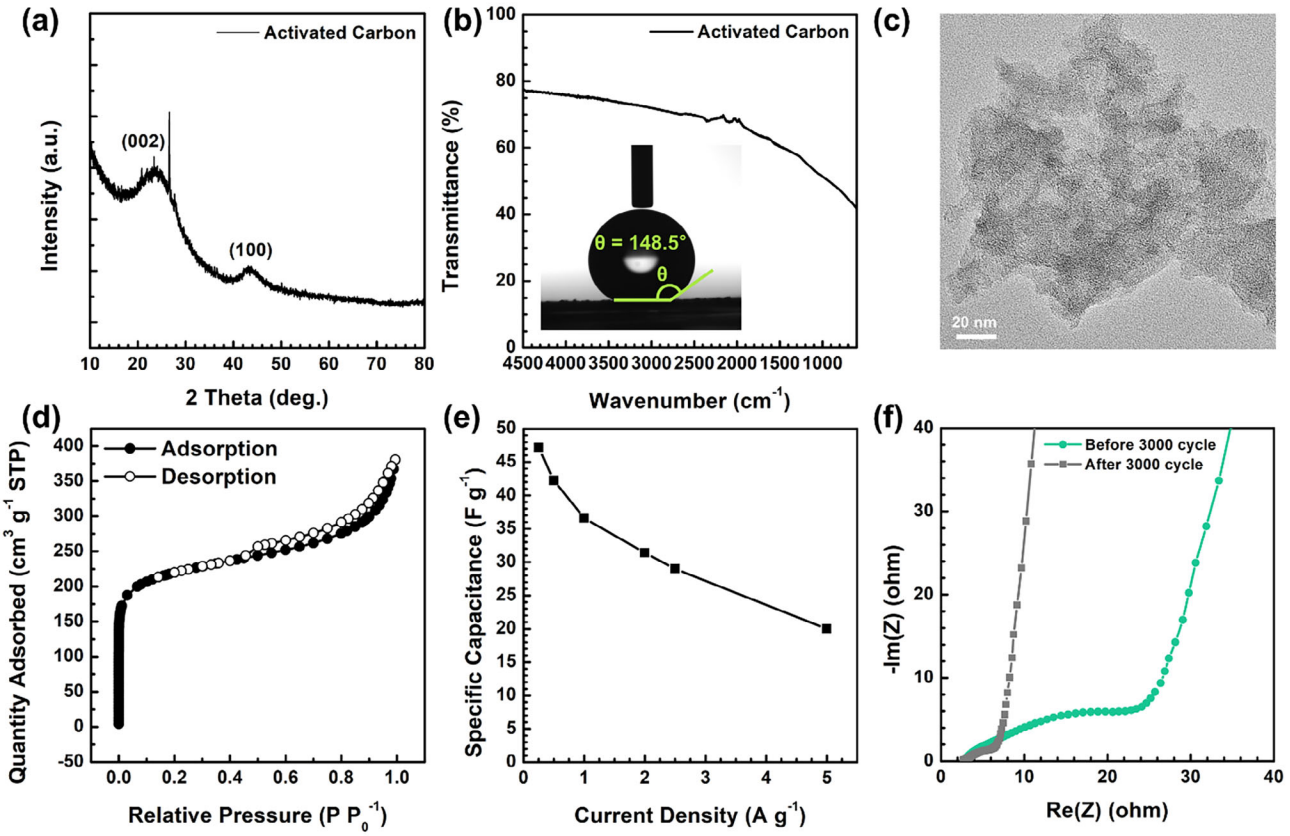

FIGURE 6 | (a) XRD pattern, (b) FT-IR spectrum and contact angle data (inset), (c) TEM image, (d) N_2 adsorption-desorption isotherm at 77 K, (e) specific discharge capacitances at current densities of 0.25, 0.50, 1.0, 2.0, 2.5, and 5.0 A g^{-1}, and (f) Nyquist plot at open circuit potential of activated carbon.

TABLE 1 | Comparison of the characteristics of δ-MnO_2@C and activated carbon.

	δ-MnO_2@C	Activated carbon	Comparison with activated carbon
Surface area	122.2 m^2 g^{-1}	751.8 m^2 g^{-1}	Decreased by 6.152-fold
Total pore volume	0.530 cm^3 g^{-1}	0.588 cm^3 g^{-1}	Decreased by 1.11-fold
Hydrophobic surface	136.4°	148.5°	Decreased by 1.09-fold
Gravimetric capacitance[a]	177.7 F g^{-1}	47.1 F g^{-1}	Increased by 3.77-fold
Areal capacitance[a]	1.066 F cm^{-2}	0.367 F cm^{-2}	Increased by 2.90-fold
Average response time	63 s	89 s	Faster by 1.4-fold

[a]at a current density of 0.25 A g^{-1}

of ion-to-electron transduction typically observed when using activated carbon as a solid-contact material.

To elucidate the underlying dynamics responsible for the superior sensing kinetics of δ-MnO_2@C, a comparative study was conducted between δ-MnO_2@C, which exhibits a rapid response, and activated carbon, which shows a relatively sluggish response in potassium-ion sensing. The physicochemical properties of activated carbon were compared with those of δ-MnO_2@C, as summarized in Figure 6 and Table 1. Activated carbon possesses a graphitic structure with low crystallinity (Figure 6a) and hydrophobic surfaces with few functional groups (Figure 6b). Its highly micro- and mesoporous structure (Figure 6c) results in an exceptionally large surface area (751.8 m^2 g^{-1}, Figure 6d), which is significantly higher than that of δ-MnO_2@C (122.2 m^2 g^{-1}). The gravimetric specific capacitances of activated carbon as an electrode material for supercapacitors are 47.1, 42.3, 36.6, 31.4, 29.0, and 20.0 F g^{-1} at current densities of 0.25, 0.50, 1.0, 2.0, 2.5, and 5.0 A g^{-1}, respectively (Figure 6e).

2.6 | Mechanism of Potentiometric Sensing

Given that the performance of miniaturized sensing devices is more closely related to geometric areal capacitance than to gravimetric capacitance, the areal specific capacitances of

δ-MnO_2@C and activated carbon were compared together with other physicochemical parameters listed in Table 1. Although δ-MnO_2@C exhibits lower surface area, total pore volume, and surface hydrophobicity than activated carbon—parameters that would typically retard ion transport—the δ-MnO_2@C-based sensing strip displays a 1.4-fold faster response. This observation indicates that these textural and chemical parameters are not the dominant factors governing sensing kinetics in the present system. Instead, the observed trend correlates closely with the capacitance differences between the two solid-contact materials. Notably, δ-MnO_2@C exhibits 3.77- and 2.90-fold higher gravimetric and areal specific capacitances, respectively, compared with activated carbon. Considering that the response-time enhancement (1.40-fold) correlates more strongly with the difference in areal rather than gravimetric capacitance, it is inferred that areal specific capacitance plays a more critical role in determining the sensing kinetics of solid-contact K^+-ISEs. To further verify the correlation between response time and specific capacitance, a series of δ-MnO_2@C analogues with systematically varied carbon coating thicknesses (Figure S8) were prepared. Their response times were compared alongside areal and gravimetric specific capacitances and coating thicknesses, as plotted in Figure S9. Although no strict linear correlation is observed across all parameters, the variation in response time follows trends that are more consistent with changes in areal and gravimetric capacitances than with coating thickness alone. This result reinforces the interpretation that capacitance, rather than geometric or structural factors, governs the sensing kinetics.

The pronounced capacitance difference between δ-MnO_2@C and activated carbon originates from their distinct charge-storage mechanisms as evidenced by Dunn's method (Figure S7). Activated carbon stores charge primarily through EDLC (Figure S6), whereas δ-MnO_2@C benefits from pseudocapacitance associated with the reversible redox reactions of Mn^{4+} [54]. Collectively, these results indicate that a high areal specific capacitance, enabled by pseudocapacitance and carbon coating, is a dominant factor governing the kinetics of ion-to-electron transduction of solid-contact materials.

δ-MnO_2@C intrinsically possesses potassium-ion intercalation capability. However, under potassium-ion sensing conditions, true bulk intercalation of K^+ into the δ-MnO_2 lattice is highly unlikely because the open-circuit potential does not provide sufficient driving force for such a faradaic process. Instead, owing to its small thickness and large surface area, δ-MnO_2@C can be directly exposed to potassium ions at the K^+-ISM interface, where surface adsorption and partial surface redox reactions may occur even under open-circuit conditions. These interfacial processes can, in principle, influence the equilibrium potential of the K^+-ISE, which follows Nernstian behavior with respect to potassium-ion activity.

At this point, the second role of the solid-contact material becomes critical. The second role of the solid-contact material is to suppress potential drift originating from unavoidable charge perturbations at the ion-selective membrane/solid-contact interface. During potassium-ion sensing, small amounts of excess charge (ΔQ) may arise from interfacial adsorption, surface redox adjustment, or minor environmental changes at the solid-contact material. These charge variations are not part of the Nernstian sensing mechanism but can nonetheless influence the measured potential. The magnitude of the resulting potential change (ΔE) is governed by the interfacial capacitance (C) according to the below electrostatic relation (Equation (2).

$$\Delta E = \Delta Q \,/\, C \tag{2}$$

Therefore, when the solid-contact material exhibits a very large capacitance, even a finite ΔQ produces only a negligible ΔE. In the case of δ-MnO_2@C, the combined contributions of EDLC from the carbon component and Faradaic capacitance from the MnO_2 surface enable efficient charge accommodation with minimal potential variation. As a result, the electrode potential rapidly stabilizes at the Nernstian equilibrium value determined by potassium-ion activity, while time-dependent potential drift is effectively suppressed and a fast response is achieved.

2.7 | Considerations for Practical and Industrial Applications

For point-of-care and disposable potassium-ion diagnostic applications, critical performance requirements include high reproducibility, selectivity against interfering ions, resistance to water-layer formation, long-term potential stability over clinically relevant time scales, and reliable operation in real biological samples. The potassium-ion selectivity of the δ-MnO_2@C-based sensing strip was systematically evaluated. As shown in Figure 7a, upon the introduction of common interfering ions such as Ca^{2+}, Mg^{2+}, and Na^+ at concentrations of 1 mM into a buffer solution containing K^+ (4 mM), the sensing strip maintained a reliable and selective Nernstian response to K^+. This robust selectivity originates not only from the intrinsic selectivity of the K^+-selective membrane but also from the formation of a stable interfacial contact that suppresses water penetration at the ion-selective membrane/solid-contact interface.

To directly verify the suppression of water-layer formation, water-layer tests were conducted for the δ-MnO_2@C- and activated carbon-based sensing strips. As shown in Figure 7b, the δ-MnO_2@C-based sensing strip exhibits minimal potential drift, comparable to that observed for the activated carbon-based sensing strip, confirming that the carbon-coating effectively establishes a hydrophobic interfacial layer. Owing to this negligible water-layer formation, the sensing strip based on δ-MnO_2@C delivers stable potentiometric performance during continuous exposure to a buffer solution containing K^+ (4 mM) for 48 h (Figure 7c). This time window exceeds typical point-of-care measurement durations, thereby ensuring robust long-term stability for continuous clinical monitoring applications.

Reproducibility and real-sample validation were further evaluated using commercially available human serum (Sigma-Aldrich, Cat. No. H6914), with four independent measurements performed under identical conditions. The human serum (Sigma-Aldrich, Cat. No. H6914) is the liquid component of blood remaining after clotting and contains various constituents, including proteins (4.0–9.0%), sodium ions (100–160 mM), glucose (50–180 mg dL^{-1}), triglycerides (30–175 mg dL^{-1}), cholesterol (80–200 mg dL^{-1}), and

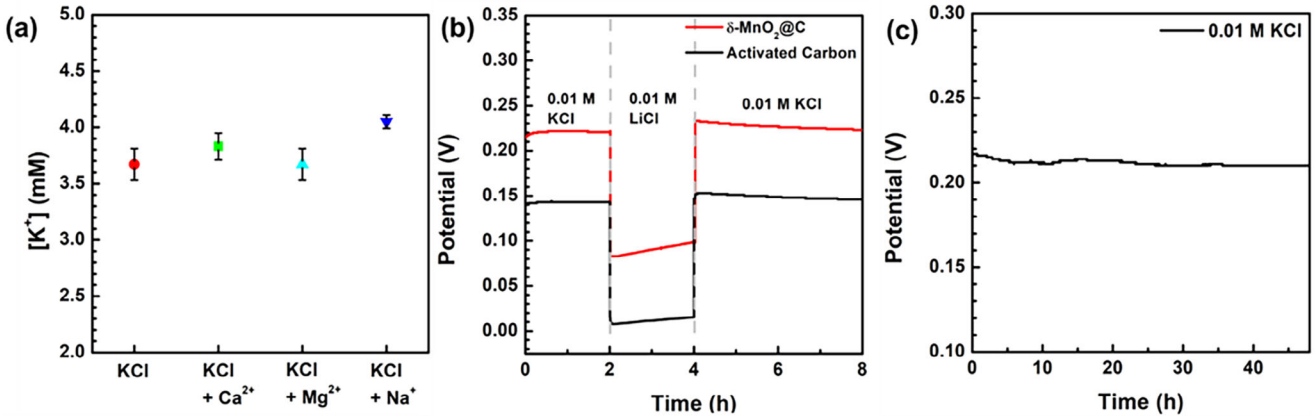

FIGURE 7 | (a) Potassium-ion selectivity of the sensing strip employing δ-MnO_2@C in the presence of 4 mM K^+ and interfering 1 mM Ca^{2+}, Mg^{2+}, and Na^+ ions (N = 4), (b) potentiometric water-layer test results for sensing strips employing δ-MnO_2@C (red) and activated carbon (black), and (c) long-term potential stability of the sensing strip employing δ-MnO_2@C under 48 h exposure conditions.

other minor minerals and biomolecules. The potassium-ion concentration measured using the δ-MnO_2@C-based sensing strip was 3.95 ± 0.23 mM, in good agreement with the value obtained by inductively coupled plasma optical emission spectroscopy (ICP-OES, 3.87 mM). These results confirm that the δ-MnO_2@C-based sensing strip accurately quantifies potassium ions in complex biological matrices despite the presence of numerous potential interferents.

In addition to electrochemical performance, low fabrication cost and simplified processing are indispensable for disposable, single-use potassium-ion sensing strips. The fabrication cost and complexity of δ-MnO_2@C were therefore benchmarked against representative solid-contact materials commonly used in potassium-ion selective electrodes, including poly(3,4-ethylenedioxythiophene):polystyrene sulfonate (PEDOT:PSS), CNT, graphene, and Au/Pt, with respect to fabrication methods, material requirements, processing steps, and relative cost. As summarized in Table S6, the δ-MnO_2@C-based solid contact offers a compelling combination of low cost, low complexity, and reliable electrochemical performance, underscoring its suitability for scalable manufacturing of point-of-care potassium-ion diagnostic devices.

3 | Conclusions

We designed and developed carbon-coated δ-MnO_2 nanosheets as an electrode material for supercapacitors and as a solid-contact material for portable self-testing potentiometric potassium-ion biosensors. Oxamide serves as an effective precursor for synthesizing a highly homogeneous carbon coating on δ-MnO_2 nanosheets. Upon oxidation by persulfate, oxamide decomposes and provides carbon and nitrogen sources for the formation of an N-doped carbon coating during the one-pot crystallization of δ-MnO_2. The large pseudocapacitance of δ-MnO_2@C, when used as an electrode material for supercapacitors, underlies its rapid ion-to-electron transduction property as a solid-contact material in potassium-ion biosensors. Notably, the practical application of δ-MnO_2@C as a solid-contact material in a portable potentiometric potassium-ion biosensor was successfully demonstrated. As shown in Video S1, the δ-MnO_2@C-employed sensing strip enables faster quantification than the activated carbon-based strip when analyzing PBS solution containing 4 mM K^+, the normal physiological potassium-ion concentration.

The present study strongly demonstrates that the large areal specific capacitance of the solid-contact material is critical for shortening response time in all-solid-state potassium-ion biosensors, and highlights the significant potential to develop superior solid-contact materials through interdisciplinary research spanning the fields of supercapacitors and biosensors. By combining rapid response, high sensitivity, and low sample volume requirements, the δ-MnO_2@C-based sensing strip represents a promising platform for cost-effective, portable potassium-ion monitoring in both clinical and at-home applications.

4 | Experimental Methods

4.1 | Synthesis

For synthesis of δ-MnO_2@C, manganese(II) acetate tetrahydrate (0.2783 mol) was dissolved in 800.0 mL of 94% ethanol under stirring at 70°C. Oxamide (0.02227 mol) was then added to the above solution, and all precursors were completely dissolved by continuous stirring at 70°C. The ethanol solvent was rotary-evaporated to concentrate the solution, and the resulting gel was completely dried in a convection oven at 76°C. The dried intermediate was finely ground into powder. Subsequently, 1.000 g of the intermediate powder was dispersed in 80.0 mL of 0.5 M ammonium persulfate solution by stirring for 24 h at 25°C. The formed precipitate was collected and washed with distilled water by centrifugation until the supernatant reached pH 7.0. The final product was dried in a vacuum oven at 25°C. A series of δ-MnO_2@C analogues with systematically varied carbon coating thicknesses was prepared by controlling the oxamide amount (0, 0.01114, and 0.04454 mol). The reference activated carbon (DARCO, ~100 mesh particle size) was purchased and used without further purification. Another reference material, δ-MnO_2, was synthesized by stirring manganese(II) acetate tetrahydrate in 0.5 M ammonium persulfate solution for 24 h at 25 °C, followed by dialysis with deionized water until the pH reached 7.0, and subsequent freeze-drying. For the potassium-ion sensing tests,

PBS (Cat. no. P5493, pH 7.2–7.6 at 25°C) and human serum (Cat. no. H6914) were purchased from Sigma-Aldrich and used as received.

4.2 | Characterization

The crystal structure of the samples was characterized by powder XRD (Rigaku, SmartLab SE, λ = 1.5418 Å), and their crystal morphology was observed by FE-SEM (JEOL, JSM-7610F) equipped with an energy-dispersive X-ray spectrometer. Textural parameters, including BET surface area and pore size, were analyzed at 77 K on an N_2 sorption analyzer (Micromeritics, ASAP 2020). Crystal structure and lattice fringes were further examined by HR-TEM/SAED (JEOL, JEM-2100F, 200 kV). Focused ion beam milling was performed on δ-MnO_2@C embedded in resin to prepare cross-sectional specimens. CHNS analysis was performed at 950°C under an oxygen atmosphere using a FlashSmart CHNS/O (ThermoFisher Scientific). Micro-Raman spectrum of δ-MnO_2@C was acquired using a LabRAM Soleil Raman microscope (Horiba Jobin Yvon) with a 532 nm excitation laser operated at a power below 0.1 mW at the Raman Research Institute, Republic of Korea. Chemical bonds were identified using FT-IR spectroscopy (Bruker, INVENIO-R). XPS was conducted on a NEXSA instrument (Thermo Fisher Scientific, Al K_α X-ray 1486.7 eV) at the GIST Advanced Institute of Instrumental Analysis (GAIA) to analyze the chemical bonding of δ-MnO_2@C. The contact angle of a water droplet on the sample surface was measured using a contact angle meter (Kruss, DSA 25). For the contact angle measurement, the samples were prepared in ink form and coated on a flat substrate using a doctor blade. ICP-OES (PerkinElmer, OPTIMA 8300) was used to quantify potassium ions in human serum. Prior to ICP-OES analysis, the human serum was diluted with a 5% HNO_3 solution.

4.3 | Ink Preparation

Powder samples (δ-MnO_2@C, δ-MnO_2, or activated carbon, 2.400 g) were dispersed in 20.0 mL of N-methyl-2-pyrrolidone by stirring at 60°C for 4 h. Carbon black (0.600 g) was then added, followed by additional stirring for 4 h. Finally, poly(vinylidene fluoride) (0.800 g) was added and completely dissolved by stirring overnight, yielding a homogeneous ink.

4.4 | Fabrication of the All-Solid-State Potassium-Ion Sensing Strips

The fabrication procedure for all-solid-state potassium-ion sensing strips was conducted according to previously reported studies [59]. The all-solid-state potassium-ion sensing strips were fabricated by screen-printing the ink onto a pre-patterned electrode substrate, followed by thermal treatment to cure the printed layer. Subsequently, an Ag/AgCl reference electrode was formed via electrochemical deposition using an $FeCl_3$ solution. The K^+-ISM was deposited onto the working electrode by a static casting method. The K^+-ISM consisted of a poly(vinyl chloride) matrix, a plasticizer, a potassium ionophore, and a lipophilic anionic additive, following commonly used formulations. After casting, the membrane was allowed to dry at 25°C.

4.5 | Electrochemical Measurements

CV and galvanostatic charge–discharge measurements were carried out in a three-electrode system using a battery cycler (Biologic, MPG-200). An Ag/AgCl (3.0 M NaCl) electrode and a platinum mesh served as the reference and counter electrodes, respectively. The sample ink-cast Ni foam (1 cm × 1 cm) was used as the working electrode. The electrolyte was 1.0 M Na_2SO_4 aqueous solution. The potential window for CV measurements was -0.100–0.900 V vs. Ag/AgCl. Galvanostatic charge–discharge measurements were performed at current densities of 0.25–5.0 A g^{-1} in the potential range of -0.100 to 0.900 V vs. Ag/AgCl. The specific capacitance was calculated using Equation (3):

$$C_{sp} = \frac{I\Delta t}{m\Delta V} \tag{3}$$

where I was the applied current (A), Δt was the discharge time (s), m was the mass of active material (g), and ΔV was the applied potential window (V). EIS was conducted in the frequency range from 100 kHz to 0.01 Hz at open circuit potential by applying an AC voltage with 5 mV amplitude. Dunn's method was applied to CV profiles recorded over a range of scan rates to quantify the relative contributions of capacitive (surface-controlled) and diffusion-controlled processes, according to Equation (4) [60]:

$$i\,(\mathrm{V}) = k_1\nu + k_2\nu^{1/2} \tag{4}$$

where $i(V)$ was the current at a given potential V, ν was the scan rate, $k_1\nu$ represents the surface-controlled (capacitive) current contribution, and $k_2\nu^{1/2}$ corresponds to the diffusion-controlled current contribution. The parameters k_1 and k_2 were constants determined from the slope CV data. To extract k_1 and k_2, Equation (4) was rearranged to Equation (5):

$$i\,(\mathrm{V})\,/\nu^{1/2} = k_1\nu^{1/2} + k_2 \tag{5}$$

Linear fitting of $i(V)/\nu^{1/2}$ vs. $\nu^{1/2}$ at a fixed potential yields k_1 as the slope and k_2 as the intercept. These constants quantify the relative magnitudes of the surface-controlled and diffusion-controlled charge-storage contributions, respectively, enabling separation of their contributions at each scan rate.

For potassium ion-dependent amperometry, the δ-MnO_2@C ink was loaded onto a glassy carbon electrode and used as the working electrode. Tris-HCl buffer solutions (pH 7.4) containing KCl (2.0–7.0 mM) served as the electrolyte. An Ag/AgCl (3.0 M NaCl) electrode and a platinum wire were used as reference and counter electrodes, respectively. CV was performed in the potential range -0.200 to 0.800 V vs. Ag/AgCl at a scan rate of 50 mV s^{-1} using the Biologic MPG-200 battery cycler.

For potentiometric tests, the fabricated all-solid-state potassium-ion sensing strip was used. Chronopotentiometric data were recorded using an all-solid-state potentiometric potassium-ion biosensor developed in this work. PBS solution (10 µL) with different KCl concentrations (4.0×10^{-3} – 6.0×10^{-3} M) were dropped on the sensing strip. The equilibrium open-circuit potential was defined as the point at which ΔE was less than ±0.1 mV over 10 s.

Selectivity tests were performed to evaluate the influence of coexisting ions on the potentiometric response of the potassium-ion sensing strip. Measurements were conducted in a PBS solution containing 4.0 mM KCl, into which $CaCl_2$, $MgCl_2$, and NaCl were individually introduced at a concentration of 1.0 mM. The potential was recorded after reaching equilibrium under each condition.

Water-layer formation tests were carried out using a sequential electrolyte exchange method to assess interfacial stability. Sensing strips employing activated carbon or δ-MnO_2@C as the solid-contact layer were investigated. Each strip was initially immersed in a 0.01 M KCl solution for 2 h, subsequently transferred to a 0.01 M LiCl solution for 2 h, and then returned to a 0.01 M KCl solution for an additional 2 h, followed by continuous measurement for 4 h. Potential changes were continuously recorded throughout the entire measurement period.

Long-term stability tests were conducted using sensing strips employing δ-MnO_2@C as the solid-contact material. Chronopotentiometric measurements were performed during continuous exposure to a 0.01 M KCl solution for 48 h, and the resulting potential drift over time was recorded to evaluate signal stability.

Human serum validation was performed by directly comparing potassium-ion concentrations determined using the δ-MnO_2@C-based potentiometric sensing strip with those measured by ICP-OES. Human serum was used as received. Measurements were performed independently four times to assess reproducibility. All electrochemical measurements were conducted at 25 °C.

Acknowledgements

This work was supported by the Seoul R&D Program through the Seoul Business Agency (SBA) (BT230224), the National Research Foundation of Korea (NRF) grant funded by the Korean Government (MSIT) (No. RS-2024-00350241; RS-2024-00397807; RS-2025-25442252), the Korea Basic Science Institute (National Research Facilities and Equipment Center) funded by the Ministry of Education (2020R 1A 6C 101B194), and the Ewha Womans University Research Grant of 2022.

Conflicts of Interest

The authors declare no conflict of interest.

Data Availability Statement

The data that support the findings of this study are available from the corresponding author upon reasonable request.

References

1. R. W. Schrier, W. Wang, B. Poole, and A. Mitra, "Acute Renal Failure: Definitions, Diagnosis, Pathogenesis, and Therapy," *Journal of Clinical Investigation* 114 (2004): 5–14, https://doi.org/10.1172/jci22353.

2. A. Francis, M. N. Harhay, A. C. M. Ong, et al., "Chronic Kidney Disease and the Global Public Health Agenda: an International Consensus," *Nature Reviews Nephrology* 20 (2024): 473–485, https://doi.org/10.1038/s41581-024-00820-6.

3. C. P. Kovesdy, "Epidemiology of Chronic Kidney Disease: an Update 2022," *Kidney International Supplements* 12 (2022): 7–11, https://doi.org/10.1016/j.kisu.2021.11.003.

4. L. A. Frassetto, A. Goas, R. Gannon, S. A. Lanham-New, and H. Lambert, "Potassium," *Advances in Nutrition* 14 (2023): 1237–1240, https://doi.org/10.1016/j.advnut.2023.06.004.

5. H. K. Walker, W. D. Hall, and J. W. Hurst, Clinical Methods: The History, Physical, and Laboratory Examinations (1990).

6. A. Sigel, H. Sigel, and R. K. O. Sigel, in *Interrelations between Essential Metal Ions and Human Diseases, Metal Ions in Life Science* (Springer, 2013).

7. T. Hutter, T. S. Collings, G. Kostova, and F. E. Karet Frankl, "Point-of-Care and Self-Testing for Potassium: Recent Advances," *Sensors & Diagnostics* 1, no. 4 (2022): 614–626, https://doi.org/10.1039/d2sd00062h.

8. E. Bakker, "Selectivity of Liquid Membrane Ion-Selective Electrodes," *Electroanalysis* 9 (1997): 7–12, https://doi.org/10.1002/elan.1140090103.

9. J. Bobacka, T. Lindfors, M. McCarrick, A. Ivaska, and A. Lewenstam, "Single-piece all-solid-state Ion-selective Electrode," *Analytical Chemistry* 67 (1995): 3819–3823, https://doi.org/10.1021/ac00116a034.

10. S. M. Armas, A. J. Manhan, O. Younce, P. Calvo-Marzal, and K. Y. Chumbimuni-Torres, "Ready-to-Use Single-Strip Paper Based Sensor for Multiplex Ion Detection," *Sensors and Actuators B: Chemical* 255 (2018): 1781–1787, https://doi.org/10.1016/j.snb.2017.08.194.

11. L. van de Velde, E. d'Angremont, and W. Olthuis, "Solid Contact Potassium Selective Electrodes for Biomedical Applications—A Review," *Talanta* 160 (2016): 56–65, https://doi.org/10.1016/j.talanta.2016.06.050.

12. L. Wei and G. Yushin, "Electrical Double Layer Capacitors with Activated Sucrose-Derived Carbon Electrodes," *Carbon* 49, no. 14 (2011): 4830–4838, https://doi.org/10.1016/j.carbon.2011.07.003.

13. Y. E. Chipangura, B. D. Spindler, P. Buhlmann, and A. Stein, "Design Criteria for Nanostructured Carbon Materials as Solid Contacts for Ion-Selective Sensors," *Advanced Materials* 36 (2024): 2309778, https://doi.org/10.1002/adma.202309778.

14. J. Bobacka, A. Ivaska, and A. Lewenstam, "Potentiometric Ion Sensors," *Chemical Reviews* 108 (2008): 329–351, https://doi.org/10.1021/cr068100w.

15. N. Lenar, R. Piech, and B. Paczosa-Bator, "High Capacity Nanocomposite Layers Based on Nanoparticles of Carbon Materials and Ruthenium Dioxide for Potassium Sensitive Electrode," *Materials* 14, no. 5 (2021): 1308, https://doi.org/10.3390/ma14051308.

16. N. Lenar, R. Piech, J. Wyrwa, and B. Paczosa-Bator, "Potassium-Selective Solid-Contact Electrode with High-Capacitance Hydrous Iridium Dioxide in the Transduction Layer," *Membranes* 11 (2021): 259, https://doi.org/10.3390/membranes11040259.

17. Y. Li, J. Li, and W. Qin, "All-Solid-State Polymeric Membrane Ion-Selective Electrodes Based on $NiCo_2S_4$ as a Solid Contact," *Analytical Chemistry* 94 (2022): 3574–3580, https://doi.org/10.1021/acs.analchem.1c04748.

18. X. Zeng and W. Qin, "A Solid-Contact Potassium-Selective Electrode with MoO_2 Microspheres as Ion-to-Electron Transducer," *Analytica Chimica Acta* 982 (2017): 72–77, https://doi.org/10.1016/j.aca.2017.05.032.

19. Y. Tang, L. Zhong, Y. Zhang, et al., "A Mixed Electronic-Ionic Conductor-Based Bifunctional Sensing Layer beyond Ionophores for Sweat Electrolyte Monitoring," *Science Bulletin* 68 (2023): 3181–3191, https://doi.org/10.1016/j.scib.2023.10.011.

20. S. Komaba, T. Akatsuka, K. Ohura, et al., "All-Solid-State Ion-Selective Electrodes with Redox-Active Lithium, Sodium, and Potassium Insertion Materials as the Inner Solid-Contact Layer," *The Analyst* 142 (2017): 3857–3866, https://doi.org/10.1039/C7AN01068K.

21. K. Tsuchiya, T. Akatsuka, Y. Abe, and S. Komaba, "Design of all-Solid-State Chloride and Nitrate Ion-Selective Electrodes Using Anion Insertion Materials of Electrodeposited Poly(Allylamine)-MnO_2 Composite," *Electrochimica Acta* 389 (2021): 138749, https://doi.org/10.1016/j.electacta.2021.138749.

22. L. Zhao, Y. Jiang, J. Hao, H. Wei, W. Zheng, and L. Mao, "Graphdiyne Oxide Enhances the Stability of Solid Contact-Based Ion Selective Elec-

trodes for Excellent in Vivo Analysis," *Science China Chemistry* 62 (2019): 1414–1420, https://doi.org/10.1007/s11426-019-9516-5.

23. Y. Shao, Y. Ying, and J. Ping, "Recent Advances in Solid-Contact Ion-Selective Electrodes: Functional Materials, Transduction Mechanisms, and Development Trends," *Chemical Society Reviews* 49 (2020): 4405–4465, https://doi.org/10.1039/C9CS00587K.

24. S. Liu, K. Liu, K. Chen, et al., "Tailoring the Structure of Supported δ-MnO_2 Nanosheets to Raise Pseudocapacitance by Surface-modified Carbon Cloth," *Journal of Power Sources* 449 (2020): 227507, https://doi.org/10.1016/j.jpowsour.2019.227507.

25. D. Malavekar, S. Pujari, S. Jang, S. Bachankar, and J. Y. Kim, "Recent Development on Transition Metal Oxides-Based Core–Shell Structures for Boosted Energy Density Supercapacitors," *Small* 20 (2024): 2312179, https://doi.org/10.1002/smll.202312179.

26. S. Sharma, G. Kaur, B. Sharma, B. N. Saiteja, and A. Dalvi, "High-performance, High Energy Density Symmetric Supercapacitors Based on δ-MnO_2 Nanoflower Electrodes Incorporated with an Ion-conducting Polymer," *RSC Advances* 14, no. 48 (2024): 35657–35670, https://doi.org/10.1039/D4RA05670A.

27. D.-Y. Sung, I. Y. Kim, T. W. Kim, M.-S. Song, and S.-J. Hwang, "Room Temperature Synthesis Routes to the 2D Nanoplates and 1D Nanowires/Nanorods of Manganese Oxides with Highly Stable Pseudocapacitance Behaviors," *The Journal of Physical Chemistry C* 115 (2011): 13171–13179, https://doi.org/10.1021/jp202041g.

28. S. J. Gregg and K. S. W. Sing, in *Adsorption, Surface Area and Porosity*, 2nd ed.,(Academic Press, 1982).

29. A. Ramakrishnan, S. Swaminathan, J. Mayandi, and K. G. Deepa, "Template Free Synthesis of Vacancy Tailored, Highly Mesoporous One-dimensional δ-MnO_2 for Energy Storage Applications," *Nano Express* 5 (2024): 015024, https://doi.org/10.1088/2632-959X/ad2fd3.

30. S. Zainab, S. Fraz, S. U. Awan, D. Hussain, S. Rizwan, and W. Mehmood, "Optimized Time Dependent Exfoliation of Graphite for Fabrication of Graphene/GO/GrO Nanocomposite Based Pseudo-Supercapacitor," *Scientific Reports* 13 (2023): 14218, https://doi.org/10.1038/s41598-023-41309-9.

31. T. W. Scharf and I. L. Singer, "Thickness of Diamond-Like Carbon Coatings Quantified with Raman Spectroscopy," *Thin Solid Films* 440 (2003): 138–144, https://doi.org/10.1016/S0040-6090(03)00703-X.

32. C. M. Julien and A. Mauger, "Nanostructured MnO_2 as Electrode Materials for Energy Storage," *Nanomaterials* 7 (2017): 396, https://doi.org/10.3390/nano7110396.

33. G. P. Anipsitakis and D. D. Dionysiou, "Radical Generation by the Interaction of Transition Metals with Common Oxidants," *Environmental Science & Technology* 38 (2004): 3705–3712, https://doi.org/10.1021/es035121o.

34. I. Y. Kim, J. M. Lee, T. W. Kim, et al., "A Strong Electronic Coupling between Graphene Nanosheets and Layered Titanate Nanoplates: A Soft-Chemical Route to Highly Porous Nanocomposites with Improved Photocatalytic Activity," *Small* 8, no. 7 (2012): 1038–1048, https://doi.org/10.1002/smll.201101703.

35. D.-Y. Sung, J. L. Gunjakar, T. W. Kim, I. Y. Kim, Y. R. Lee, and S.-J. Hwang, "Graphene-Assisted Room-Temperature Synthesis of 2D Nanostructured Hybrid Electrode Materials: Dramatic Acceleration of the Formation Rate of 2D Metal Oxide Nanoplates Induced by Reduced Graphene Oxide Nanosheets," *Chemistry—A European Journal* 19 (2013): 7109–7117, https://doi.org/10.1002/chem.201300001.

36. I. Y. Kim, Y. K. Jo, J. M. Lee, L. Wang, and S.-J. Hwang, "Unique Advantages of Exfoliated 2D Nanosheets for Tailoring the Functionalities of Nanocomposites," *The Journal of Physical Chemistry Letters* 5 (2014): 4149–4161, https://doi.org/10.1021/jz502038g.

37. F. S. Parker, in *Applications of Infrared Spectroscopy in Biochemistry*. 1st ed. (Springer, 1971).

38. M. Margoshes and V. A. Fassel, "The Infrared Spectra of Aromatic Compounds," *Spectrochimica Acta* 7 (1955): 14–24, https://doi.org/10.1016/0371-1951(55)80003-3.

39. U.-A. Kanta, V. Thongpool, W. Sangkhun, N. Wongyao, and J. Wootthikanokkhan, "Preparations, Characterizations, and a Comparative Study on Photovoltaic Performance of Two Different Types of Graphene/TiO_2 Nanocomposites Photoelectrodes," *Journal of Nanomaterials* 2017 (2017): 1, https://doi.org/10.1155/2017/2758294.

40. H. Bae, T. Ahmad, I. Rhee, Y. Chang, S.-U. Jin, and S. Hong, "Carbon-Coated Iron Oxide Nanoparticles as Contrast Agents in Magnetic Resonance Imaging," *Nanoscale Research Letters* 7 (2012): 44, https://doi.org/10.1186/1556-276X-7-44.

41. P. Lazar, R. Mach, and M. Otyepka, "Spectroscopic Fingerprints of Graphitic, Pyrrolic, Pyridinic, and Chemisorbed Nitrogen in N-Doped Graphene," *The Journal of Physical Chemistry C* 123 (2019): 10695–10702, https://doi.org/10.1021/acs.jpcc.9b02163.

42. S. Wang, L. A. L. Tang, Q. Bao, et al., "Room-Temperature Synthesis of Soluble Carbon Nanotubes by the Sonication of Graphene Oxide Nanosheets," *Journal of the American Chemical Society* 131 (2009): 16832–16837, https://doi.org/10.1021/ja905968v.

43. Z. Nie, Y. Huang, B. Ma, et al., "Nitrogen-Doped Carbon with Modulated Surface Chemistry and Porous Structure by a Stepwise Biomass Activation Process towards Enhanced Electrochemical Lithium-Ion Storage," *Scientific Reports* 9 (2019): 15032, https://doi.org/10.1038/s41598-019-50330-w.

44. A. Ghosh, S. Ghosh, G. M. Seshadhri, and S. Ramaprabhu, "Green Synthesis of Nitrogen-Doped Self-Assembled Porous Carbon-Metal Oxide Composite towards Energy and Environmental Applications," *Scientific Reports* 9 (2019): 5187, https://doi.org/10.1038/s41598-019-41700-5.

45. Z. Xing, Z. Ju, Y. Zhao, et al., "One-Pot Hydrothermal Synthesis of Nitrogen-Doped Graphene as High-Performance Anode Materials for Lithium Ion Batteries," *Scientific Reports* 6 (2016): 26146, https://doi.org/10.1038/srep26146.

46. N. P. D. Ngidi, A. F. Koekemoer, and S. S. Ndlela, "Recent Advancement in the Electrochemical Performance of Electrochemical Capacitors Based on Biomass-Derived Porous Carbon: a Review," *Journal of Energy Storage* 89 (2024): 111638, https://doi.org/10.1016/j.est.2024.111638.

47. P. Iamprasertkun, A. Krittayavathananon, A. Seubsai, et al., "Charge Storage Mechanisms of Manganese Oxide Nanosheets and N-Doped Reduced Graphene Oxide Aerogel for High-Performance Asymmetric Supercapacitors," *Scientific Reports* 6 (2016): 37560, https://doi.org/10.1038/srep37560.

48. Y. Zhang, X. Han, Z.-H. Huang, et al., "Shielding Mn 3^+ Disproportionation with Graphitic Carbon-Interlayered Manganese Oxide Cathodes for Enhanced Aqueous Energy Storage System," *Small* 20 (2024): 2401849, https://doi.org/10.1002/smll.202401849.

49. J.-P. Veder, R. De Marco, G. Clarke, et al., "Elimination of Undesirable Water Layers in Solid-Contact Polymeric Ion-Selective Electrodes," *Analytical Chemistry* 80 (2008): 6731–6740, https://doi.org/10.1021/ac800823f.

50. R. A. Davoglio, G. Cabello, J. F. Macro, and S. R. Biaggio, "Synthesis and Characterization of α-MnO_2 Nanoneedles for Electrochemical Supercapacitors," *Electrochimica Acta* 261 (2018): 428–435, https://doi.org/10.1016/j.electacta.2017.12.118.

51. L. Athouël, F. Moser, R. Dugas, O. Crosnier, D. Belanger, and T. Brousse, "Variation of the MnO_2 Birnessite Structure Upon Charge/Discharge in an Electrochemical Supercapacitor Electrode in Aqueous Na_2SO_4 Electrolyte," *The Journal of Physical Chemistry C* 112 (2008): 7270–7277, https://doi.org/10.1021/jp0773029.

52. S. Kour, S. Tanwar, and A. L. Sharma, "MnO_2 Nanorod Loaded Activated Carbon for High-Performance Supercapacitors," *Journal of Alloys and Compounds* 910 (2022): 164834, https://doi.org/10.1016/j.jallcom.2022.164834.

53. N. A. Salleh, S. Kheawhom, and A. A. Mohamad, "Characterizations of Nickel Mesh and Nickel Foam Current Collectors for Supercapacitor

Application," *Arabian Journal of Chemistry* 13 (2020): 6838–6846, https://doi.org/10.1016/j.arabjc.2020.06.036.

54. A. C. Lazanas and M. I. Prodromidis, "Electrochemical Impedance Spectroscopy—A Tutorial," *ACS Measurement Science Au* 3 (2023): 162–193, https://doi.org/10.1021/acsmeasuresciau.2c00070.

55. S. Kim, M. Hankel, W. Cha, et al., "Theoretical and Experimental Investigations of Mesoporous C_3N_5/MoS_2 Hybrid for Lithium and Sodium Ion Batteries," *Nano Energy* 72 (2020): 104702, https://doi.org/10.1016/j.nanoen.2020.104702.

56. J. Krämer, R. Kang, L. M. Grimm, L. De Cola, P. Picchetti, and F. Biedermann, "Molecular Probes, Chemosensors, and Nanosensors for Optical Detection of Biorelevant Molecules and Ions in Aqueous Media and Biofluids," *Chemical Reviews* 122 (2022): 3459–3636, https://doi.org/10.1021/acs.chemrev.1c00746.

57. A. S. Vedpathak, M. A. Desai, S. Bhagwat, and S. D. Sartale, "Green Strategy for the Synthesis of K^+ Pre-Inserted MnO_2/rGO and Its Electrochemical Conversion to Na-MnO_2/rGO for High-Performance Supercapacitors," *Energy & Fuels* 36 (2022): 4596–4608, https://doi.org/10.1021/acs.energyfuels.2c00381.

58. W. Gao, X. Xie, and E. Bakker, "Direct Potentiometric Sensing of Anion Concentration (Not Activity)," *ACS Sensors* 5 (2020): 313–318, https://doi.org/10.1021/acssensors.9b02523.

59. J. Yang, J. Cheng, Z. Chu, X. Luo, D. Li, and J. Guo, "Handheld Micro Blood Potassium Detection Device Based on Paper-based Ion-selective Electrodes," *Measurement* 253 (2025): 117476, https://doi.org/10.1016/j.measurement.2025.117476.

60. S. Harish and P. U. Sathyakam, "Dunn's Method for Distinguishing Charge Storage Mechanisms in Supercapacitors: a Status Quo Review," *Journal of Electronic Materials* 54 (2025): 10858–10872, https://doi.org/10.1007/s11664-025-12481-7.

Supporting Information

Additional supporting information can be found online in the Supporting Information section.

Supporting File: smll73100-sup-0001-SuppMat.docx.

Supporting File: smll73100-sup-0002-VideoS1.mp4.